coatings

Article

Dual Synergistic Effects of MgO-GO Fillers on Degradation Behavior, Biocompatibility and Antibacterial Activities of Chitosan Coated Mg Alloy

Mohammad Zolfaghari Baghbaderani [1], Somayeh Abazari [2,3], Hamid Reza Bakhsheshi-Rad [1,*], Ahmad Fauzi Ismail [4], Safian Sharif [5], Aliakbar Najafinezhad [1], Seeram Ramakrishna [6], Mohammadreza Daroonparvar [7,*] and Filippo Berto [8,*]

[1] Advanced Materials Research Center, Department of Materials Engineering, Najafabad Branch, Islamic Azad University, Najafabad, Iran; Mohammadzolfaghari.bi@gmail.com (M.Z.B.); aliakbar.najafinejad@gmail.com (A.N.)
[2] Department of Materials and Metallurgical Engineering, Amirkabir University of Technology, Tehran, Iran; somayeh.abazari@gmail.com
[3] Iranian National Standards Organization, Tehran, Iran
[4] Advanced Membrane Technology Research Center (AMTEC), University Teknologi Malaysia, Johor Bahru 81310, Johor, Malaysia; afauzi@utm.my
[5] Faculty of Engineering, University Teknologi Malaysia, Johor Bahru 81310, Johor, Malaysia; safian@utm.my
[6] Department of Mechanical Engineering, National University of Singapore, 9 Engineering Drive 1, Singapore 117576, Singapore; seeram@nus.edu.sg
[7] Department of Chemical and Materials Engineering, University of Nevada, Reno, NV 89501, USA
[8] Department of Mechanical and Industrial Engineering, Norwegian University of Science and Technology, 7491 Trondheim, Norway
* Correspondence: rezabakhsheshi@pmt.iaun.ac.ir (H.R.B.-R.); mr.daroonparvar@yahoo.com (M.D.); filippo.berto@ntnu.no (F.B.)

Abstract: The aim of this work was to establish and characterize chitosan/graphene oxide- magnesium oxide (CS/GO-MgO) nanocomposite coatings on biodegradable magnesium-zinc-cerium (Mg-Zn-Ce) alloy. In comparison to that of pure CS coatings, all composite coatings encapsulating GO-MgO had better adhesion strength to the Mg-Zn-Ce alloy substrate. The result depicted that the co-encapsulation of GO-MgO into the CS layer leads to diminish of contact angle value and hence escalates the hydrophilic characteristic of coated Mg alloy. The electrochemical test demonstrated that the CS/GO-MgO coatings significantly increased the corrosion resistance because of the synergistic effect of the GO and MgO inside the CS coating. The composite coating escalated cell viability and cell differentiation, according to cytocompatibility tests due to the presence of GO and MgO within the CS. The inclusion of GO-MgO in CS film, on the other hand, accelerates the formation of hydroxyapatite (HA) during 14 days immersion in SBF. Immersion results, including weight loss and hydrogen evolution tests, presented that CS/GO-MgO coating enables a considerably reduced degradation rate of Mg-Zn-Ce alloy when compared to the bare alloy. In terms of antibacterial-inhibition properties, the GO-MgO/CS coatings on Mg substrates showed antibacterial activity against *Escherichia coli* (*E. coli*), with a large inhibition area around the specimens, particularly for the coating containing a higher concentration of GO-MgO. Bacterial growth was not inhibited by the bare Mg alloy samples. The CS/GO-MgO composite coating is regarded as a great film to enhance the corrosion resistance, bioactivity, and antibacterial performance of Mg alloy implants.

Keywords: magnesium alloy; composite coating; structural characterization; mechanical properties; bioactivity; antibacterial activity; biocompatibility

1. Introduction

Magnesium (Mg) and its alloys showed great potential in the manufacture of automobile components, aviation constituents, and in the human body, owing to their outstanding

mechanical properties and perfect biocompatibility. On the other hand, their current use and future development are limited due to the high degradation rate of magnesium alloys in corrosive solution containing chloride ions [1,2]. A variety of techniques were used to decrease the corrosion rate of magnesium alloys. Laser surface alloying, conversion coatings, electrochemical deposition, micro-arc oxidation, alkaline treatment, and sol-gel coatings were all proposed as surface modification techniques [2,3]. Organic polymer material composite coating via sol-gel methods were employed on the magnesium alloy surface to reduce its degradation rate and further protect Mg alloy substrate exposed to the SBF [4,5]. The bacterial infections related to implants are increasing and should not be ignored [6–8]. The mentioned infections cause high medical costs and lead to higher suffering of patients. Preparation polymer layer over the surface of Mg alloy could also increase antibacterial activity of the substrate and prevent the post infections of the body and thus expanding their use in orthopedic applications. In this respect, the antibacterial properties of chitosan (CS), a polysaccharide comprised of glucosamine and N-acetylglucosamine units, are well known. CS in bulk has a wide range of applications as an antibacterial coating layer besides its great biocompatibility, lack of toxicity, and biodegradability [6–8]. Bacterial growth was shown to be inhibited more effectively by CS–ZnO nanocomposite films [8]. Furthermore, the antibacterial performance of CS–ZnO coating (the CS coatings containing 0.05, 0.1, 0.15, and 0.2 g ZnO) against *E. coli* was demonstrated to be 1.2-fold higher than that of the CS coating without ZnO [8]. Chitosan-based composites promote the attachment of cells, cell proliferation, and differentiation due to structural similarities between chitosan and extracellular matrix structures [9]. Although CS has low mechanical strength, CS-based composites have the potential to enhance physical and chemical properties [10,11]. Furthermore, in simulated inflammatory conditions, coatings containing CS have higher adhesion strength and corrosion protection; for example, a hydroxyapatite (HA)/CS composite presented higher level of protection and greater adhesive strength than pure HA [12,13]. Hence, CS film adhesion strength, bioactivity, corrosion behavior, and antibacterial performance could be improved by adding reinforcement particles like MgO and GO [14,15].

MgO is biocompatible and can release magnesium ions, which can help human metabolism [16]. Furthermore, several studies revealed direct MgO growth on graphene due to solid interfacial bonding properties. This was suggested to be related to the strong bond between carbon and oxygen [17]. Also, MgO could construct solid interfacial bonds with the Mg matrix because of proper lattice matching, as exhibited by Y. Wang et al. [17,18]. The presence of a GO in a CS layer increases the antibacterial activity of a polymer layer containing MgO nanoparticles (NPs) [14,19,20]. Because of its exceptional mechanical, biological, chemical, and electrical characteristics, GO has found a special place in the biomedical field in addition to its applications in electronics and chemicals [21]. Because of their active functional groups, GO-modified surfaces contribute to improved protein-surface interaction, resulting in improved cell attachment and proliferation [22]. Besides, antibacterial properties and the ability to influence osteogenic differentiation are unique properties that may cause GO to become a viable material for designing advanced orthopedic devices [20]. So far, no studies were conducted on the effect of CS/MgO-GO nanocomposite coatings on corrosion behavior and antibacterial behavior of Mg alloys. In this study, CS film and CS film incorporated with MgO-GO filler were coated on the surface of Mg alloy using a dip-coating method to improve Mg alloy corrosion behavior and antibacterial performance for orthopedic applications.

2. Experimental

2.1. Materials and Method

As-cast Mg-Zn-Ce samples with 10 mm × 10 mm × 5 mm dimensions were prepared based on Ref [23]. For the coating process, CS powder with a molecular weight (MW) of 190–310 kDa, MgO NPs (both purchased from Sigma-Aldrich, Gillingham, UK), and graphene oxide (GO) powder prepared via oxidizing natural fake graphite using the

modified Hummers method [24]. MgO/GO was fabricated with a simple solvothermal method according to the Ref [25]. In 1000 mL of 2.0% acetic acid aqueous solution, chitosan (1.5 g) was dissolved. After that, MgO/GO powder with various concentration (1, 2 and 3 wt.%) was added to the CS solution; to unified mixing of the powder in the chitosan solution, the mixture was stirred for three hours with a magnetic stirrer and sonicated for 2 h (Qsonica, Q125, Power Rating = 125 W, Frequency = 20 kHz). The obtained CS/MgO-GO was deposited 3 times using a dip-coating method [2] on the surface of polished Mg alloys (Scheme 1). Each layer was dried at 40 °C for 24 h before the next layer was applied. Finally, the coated samples were rinsed with a 0.1 M NaOH solution and then distilled water to reduce the effect of acetic acid on the surfaces.
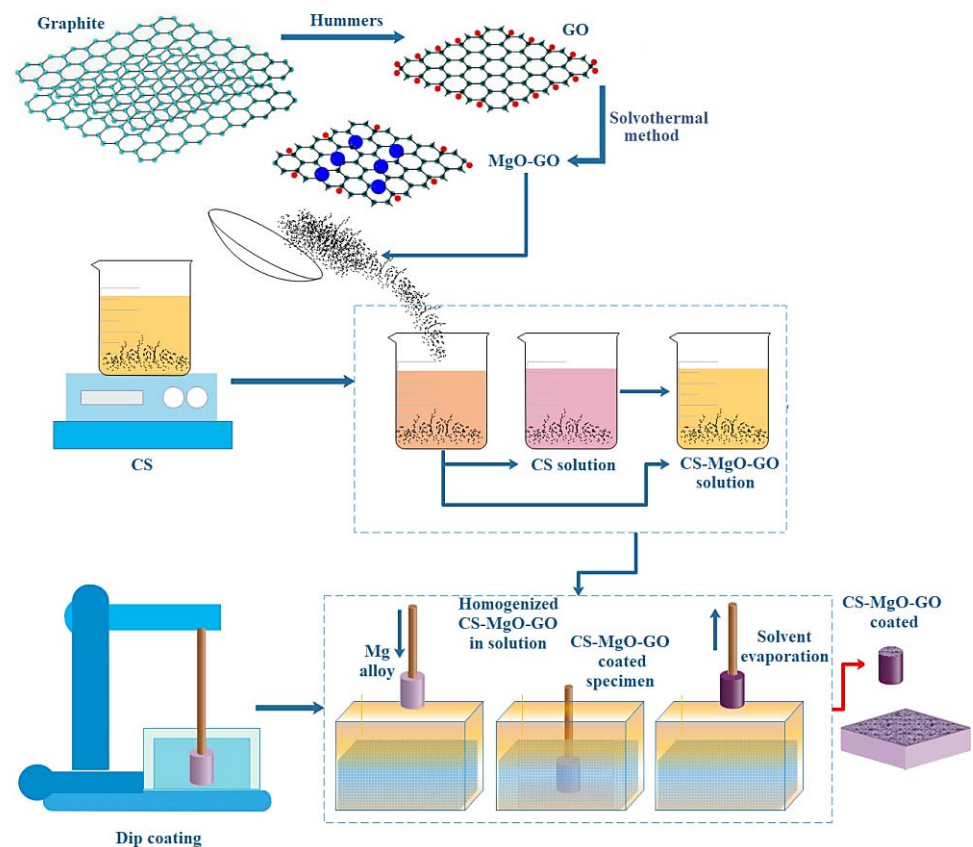
Scheme 1. Schematic of preparation process of CS/MgO-GO nanocomposite coating on Mg alloy.

2.2. Microstructural Characterization

Microstructural characterizations were performed using a field emission scanning electron microscope (FESEM, Tescan, Mira 3 Czech Republic, Prague, Czech Republic) quipped with energy dispersive spectroscopy (EDS, JSM-5910LV, JOEL Ltd., Tokyo, Japan). To reveal the phase components, X-ray diffraction (Philips PW3040, The Netherlands) with Cu-Kα radiation (30 kV, 30 mA) was used. Transmission electron microscopy (TEM; Phillips 208 m) was employed to investigate the morphology of GO nano-platelets, and MgO-GO composite powders. Fourier-transform infrared (FTIR; ALPHA-T, Bruker, Ettlingen, Germany) spectroscopy in the spectral range of 4000 to 400 cm^{-1} for detecting functional groups on the surface of coated specimens was employed. The bonding strength between the coated layer and the Mg substrate was measured at a rate of 5 mm/min using an ASTMF1044-05 universal tensile testing machine (RB 301 UNITECHM, Daejeon, Korea). A contact angle (CA) meter (GBX Digidrop, Romans-sur-Isère, France) was used to investigate the surface wettability caused by composite coating on Mg substrates. Deionized water was used in this experiment, which was carefully discharged onto the coated Mg substrates.

2.3. Corrosion Behavior

To investigate corrosion behavior, an EC-Lab machine was used to perform a potentiometric polarization test in the SBF at a voltage range of -250 to $+250$ mV$_{SCE}$ an open circuit potential at a rate of 0.5 mV/s. A graphite electrode was used as the counter electrode, and a saturated calomel electrode (SCE) was used as the reference electrode, and the samples were tested with a working electrode that had a surface area of 1 cm^2 exposed to the electrolyte. The corrosion potential, the current corrosion density, and slope of the anodic and cathode curves were also determined using the EC-Lab express software. After 30 min of specimen placement in the SBF, electrochemical impedance spectrometry (EIS) was used to achieve potential stability. Using an open circuit potential and a sine signal with a potential amplitude of 10 mV, this test was performed in accordance with the ASTM G106 standard at an open circuit potential in the range of 10^5 to 10^{-2} Hz. The samples were immersed in 200 mL of Kokubo SBF solution for the immersion test, as per ASTM G1-03 (pH 7.4). The composition of the Kokubo simulated body fluid (SBF) is presented in the supporting information (Table S1). After each 24 h interval during the immersion test, the variation in the pH value of the SBF solution (PHS-3C, Shanghai Lei Ci Device Works, China) was recorded at a constant temperature of 37 °C for 3-, 7-, and 14-day durations. The surface corrosion products of composites were cleaned with a chromic acid solution (300 g/L Cr$_2$O$_3$ + 10 g/L AgNO$_3$) prior to weight loss measurements [26]. The degradation rate was calculated using the weight loss test according to the following equation:

$$C_R = \frac{W}{A \times t \times d} \tag{1}$$

where *W*, *A*, *t*, and *d* represent weight loss (g), sample area (cm^2), exposure time (s), and density (g/cm^3). The C$_R$ unit is cm/s, which is converted to mm/year by multiplying by 3.154×10^8. To achieve repeatable results, each test was repeated three times. In addition, according to Ref. [26], the volume of H$_2$ released as a result of the magnesium dissolution was determined for 3-, 7-, and 14-day durations at a constant temperature of 37 °C. The coating containing MgO and GO were first immersed in SBF, then funneled, and an upside-down burette filled with SBF placed directly above them to trap the H$_2$ gas.

2.4. Antibacterial Activity

The antimicrobial activity against *E. coli* bacteria was determined using the disc diffusion method to study the biological behavior of each uncoated and composite coated (*n* = 3) sample. To achieve this, the sterile swab dipped in the microbial suspension was flushed (by pressing swabs against the pipe's side) and the cultivation environments were lawns. The specimens were incubated in an agar medium for 1 day at 37 °C in an incubator. According to Ref. [11], the inhibition area (IA) around the samples can reveal whether they have antibacterial properties.

2.5. In-Vitro Biocompatibility

The in vitro cytotoxicity of nanocomposite coatings, both uncoated and coated, was determined using an indirect 3-(4,5-dimethylthiazol-2-yl)-2,5-diphenyltetrazolium- bromide (MTT, Sigma, Saint Louis, MO, USA) assay based on the extraction technique. The nanocomposites coating were added to the culture medium and incubated for 3 and 5 days at 37 °C. Human osteogenic sarcoma MG-63 cells line were cultivated under the standard cell-culture conditions. The cell medium was refreshed with 3 and 5-day extracts after 10^4 cells/mL were refined on the 96-well plates for 24 h. After another 24 h, the medium was removed, and 100 mL of MTT agents (0.5 mg/mL in PBS) were inoculated into each well and kept in the incubator for 4 h. After 4 h, 100 μL of DMSO was injected into the well to dissolve the formazan crystals. Finally, the absorbance was measured at 545 nm using an ELISA Reader (Stat Fax-2100, Miami, FL, USA) and compared to a control group of free nanocomposites culture medium. The samples were washed twice and then fixed with

paraformaldehyde for alkaline phosphatase (ALP) activity tests after being cultured for 3 and 7 days, according to Ref. [11].

2.6. Statistical Analysis

The experimental data were evaluated using the program SPSS 19.0 and expressed according to the average $\pm$ standard deviation. Student t-tests were performed be-tween various groups to assess p values that were assumed to be significant when $p < 0.05$ was used.

3. Result and Discussion

3.1. Structural Characterization GO and MgO

The TEM image GO offers a flake-like shape with a thickness of almost 3–5 nm, which is higher than that of neat graphene (0.355 nm) owing to the oxygenated groups in GO as shown in Figure 1a. However, the TEM image of MgO/GO showed that the MgO possesses a spherical shape, which merged and created an agglomerate within flake-like shape of GO along with a mean particle size of almost 80–100 nm (Figure 1b). Moreover, the images show the homogenous distribution of MgO inside the GO sheets with great attachment. The homogeneous dispersion of nanofillers in the matrix, as described in the literature, is an important requirement for preparing nanocomposite coating with unique efficiency. As presented in Figure 1c, the XRD pattern of GO powder displays characteristic peaks at $2\theta = 10.03°$ and $42°$, connected to the preferable orientation (001) and (100) of GO, respectively [25,27]. The XRD patterns of the MgO/GO powder clearly show the presence of MgO, where the diffraction peaks appear at $37.50°$, $42.50°$, and $59.20°$ (JCPDS 87–0653) corresponding to the (111), (200), and (220) respectively besides to the characteristic peaks of GO (Figure 1d). The reflections from the (111), (200), (220), (311), and (222) planes of cubic MgO were recognised in the XRD peaks which presented in the supporting information (Figure S1b). Two dominant peaks were observed in the Raman spectra (Figure 1e) of the neat GO, with D and G peaks being detected between 1355 and 1582 cm^{-1}, which is aligned with the vibrational modes of the D–band caused by structural defects and the G–band of the graphic materials [25,27]. The D peak and G peak are attributed to the stretching of the in-plane C–C bond in GO. The attained I_D/I_G intensity ratio values for GO are about 0.88 [28]. FT-IR spectra of GO, and MgO–GO are shown in Figure 1f. In the curve of GO, the characteristic peaks at 3430 and 1712 cm^{-1} correspond to the stretching vibrations of O–H and C=O bands, respectively, while the peak of C–OH at 1414 cm^{-1}, the stretching peak of C–C at 1052 cm^{-1}, and the vibration peak of C=C at 1633 cm^{-1} and original peaks of C=O (1740 cm^{-1}), C–O–C (1242 cm^{-1}), and C–O (1079 cm^{-1}) is related to the GO. In the FTIR spectrum of MgO/GO, the C=C peak (1650 cm^{-1}) and C–OH peak (1401 cm^{-1}) came from GO [25,27], while the peak at 460 cm^{-1} corresponds to the vibration of the Mg–O came from MgO.

3.2. Surface Analysis

As shown in Figure 2a, the microstructure of Mg-Zn-Ce alloy consists of α-Mg and a small number of intermetallic phases, which are mainly located within grain boundaries. According to the EDS test, Mg, Zn, and Ce are the marked area constituents, possibly showing the presence of $Mg_{12}Ce$ phases (Figure 2b,c). The XRD analysis will confirm the formation of the aforementioned phases.

Figure 3 shows the FESEM micrographs of the various surfaces. Without MgO-GO, the surface of the CS-coated Mg substrate shows a smooth layer with several close pores (Figure 3a). The evaporation of organic solvent during the drying process creates these pores. The CS/(1–3)MgO-GO coating, on the other hand, has a unified surface with nano-particle size MgO-GO dispersed throughout, as well as a bubble-like structure created on the surface film (Figure 3b,c). The CS/2MgO-GO coating produced a more uniform layer with less close porosity, which has a significant impact on the corrosion behavior of the alloy. As the MgO-GO content increases, the surfaces of CS/GO films become rougher and

more porous, as shown in Figure 3d. The EDS analysis (Area A–D) revealed that these particles were mostly comprised of O and Mg elements, implying that they were MgO. Both the GO and the CS matrix were found to be encapsulated in the deposited film, which was affirmed more by the existence of carbon element.
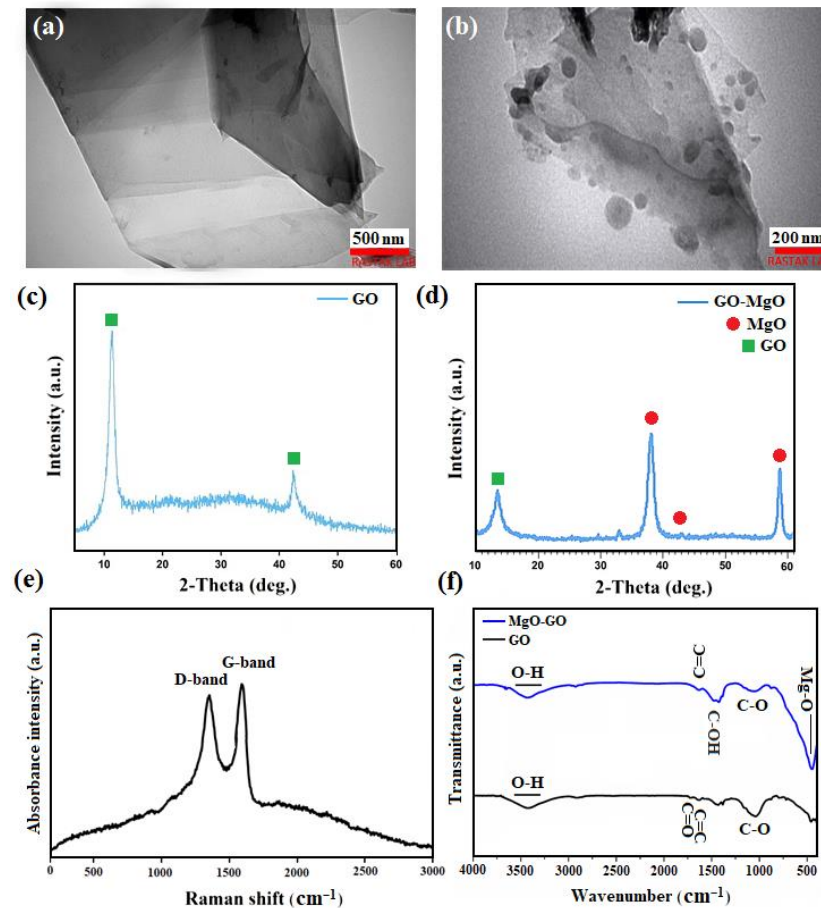

Figure 1. Transmission Electron Microscopy (TEM) images of (**a**) GO, (**b**) MgO/GO powders; X-ray Diffraction (XRD) patterns of (**c**) GO and (**d**) MgO-GO powders; and (**e**) Raman spectra of GO and (**f**) Fourier Transform Infrared (FTIR) patterns of GO and MgO-GO powders.
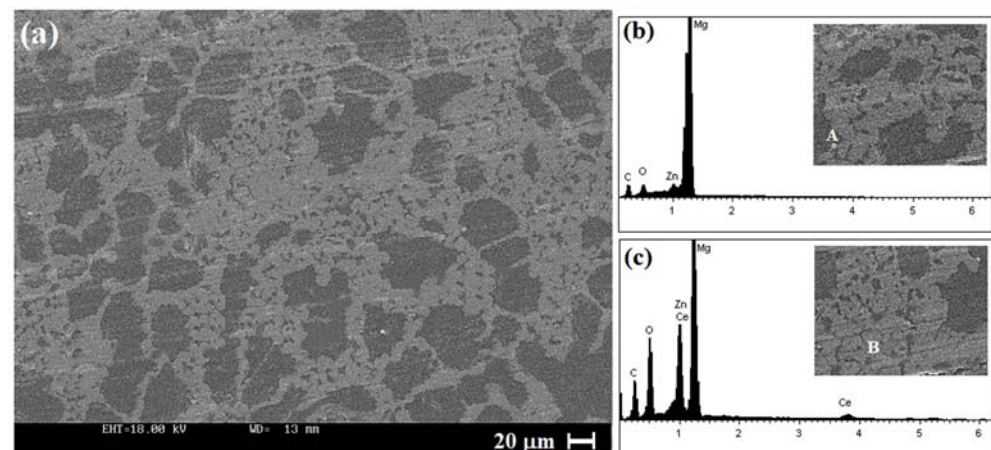

Figure 2. (**a**) Scanning Electron Microscope (SEM) micrographs of Mg-Zn-Ce alloy, and Energy Dispersive X-ray Spectroscopy (EDX) analysis of (**b**) area A and (**c**) area B.
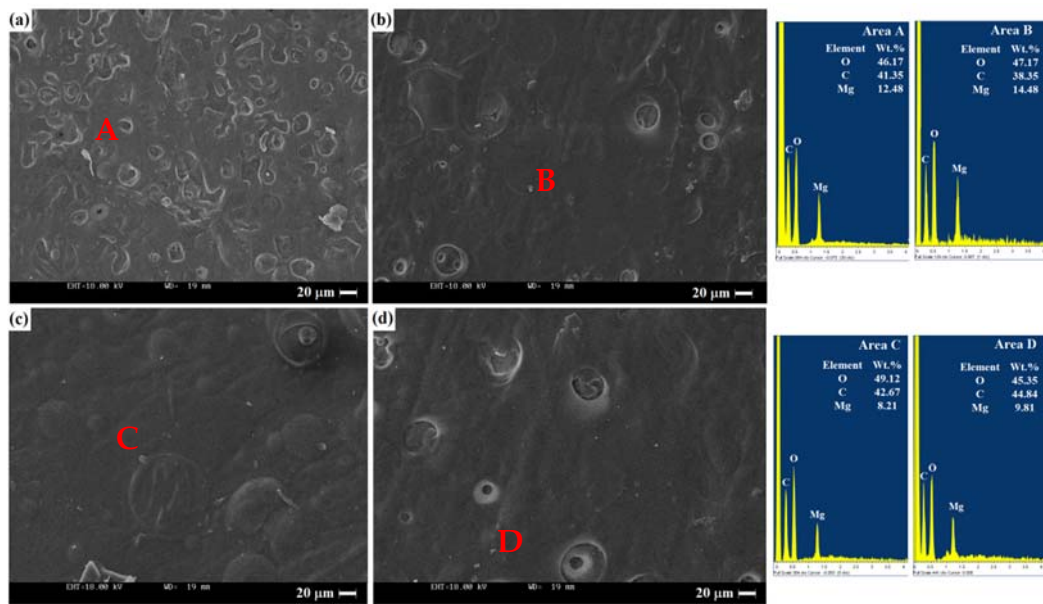
Figure 3. SEM images (**a**) CS, (**b**) CS/1MgO-GO, (**c**) CS/2MgO-GO, and (**d**) CS/3MgO-GO coated Mg alloys, and corresponding EDX analysis of Areas A, B, C, and D.

According to the XRD spectrum, the main phases in the Mg-Zn-Ce alloy are α-Mg, and $Mg_{12}Ce$ (Figure 4a). The CS coating exhibited broad peaks at $2\theta = 10°–20°$, whereas the CS/MgO-GO coating revealed the presence of an amorphous CS structure [29]. With the addition of GO and MgO, the intensity of the characteristic peak of CS decreases, indicating an increase in amorphous CS content. It was determined that the majority of the CS/MgO-GO coating was comprised of Mg and MgO. The CS/MgO-GO coating showed characteristic peaks at ~42.7° and ~62.1° related to (111) and (200) planes respectively corresponding to MgO [18,30]. Because of the coating structure, the substrate peaks were reflected in the patterns, allowing X-ray to reach the internal substrate. Commonly, the diffraction peak of GO appears around 12°, but no characteristic peak of GO was observed in this work. This could be attributed to the prepared films possess low amount of GO and also have poor crystallization [31]. In this respect, Askarnia et al. reported [12] that characteristic diffraction of graphene oxide at about $2\theta = 10°$ was not detectable due to the low content of GO in HAp/CS/GO coatings.
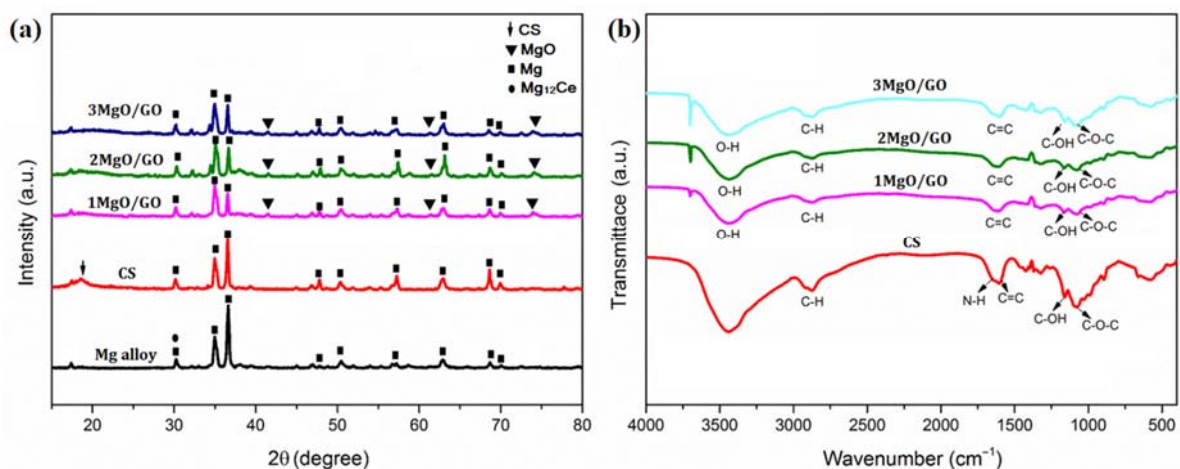

Figure 4. (**a**) XRD patterns and (**b**) FTIR analysis of CS, CS/1MgO-GO, CS/2MgO-GO, and CS/3MgO-GO coated Mg alloys.

The presence of graphene oxide, CS, and MgO in the coating was confirmed using FTIR analysis (Figure 4b). The most important bands in CS were stretching vibrations of O–H from carbohydrate rings and adsorbed water (3500–3450 cm^{-1}); N–H stretching in amine and amide ($\sim$3360 cm^{-1}); carbonyl bond (C=O) vibration in amide group at 1653 cm^{-1} and N–H bending vibration of amine group at 1580 cm^{-1} [12,32]. The peaks at 1405.8, 1153, and 1069.5 cm^{-1} correspond to the C−OH stretching vibration, C−C stretching vibration, and C−O vibration, respectively [29]. Peaks at 1047.6 and 1621.1 cm^{-1} for GO nanosheets correspond to the C−O−C stretching vibration and C−C stretching mode of the sp2 carbon skeletal network, respectively. The −OH groups in adsorbed water were responsible for the distinct peak at around 3400 cm^{-1}. Because of these oxygen-containing functional groups, GO is extremely hydrophilic [29]. As MgO increased up to 3 wt.%, a new peak at 3697 cm^{-1} was observed which is attributed to the stretching of H–O–H. It is well known that H_2O and CO_2 molecules are easily chemisorbed onto MgO surface when exposed to the atmosphere. However, as MgO concentration increased to 3 wt.%, this peak strength became stronger. The peak at 568 cm^{-1} corresponds to the vibration of the Mg–O. The FTIR spectra of CS/GO-MgO films clearly demonstrated that GO and MgO were combined in the CS matrix.

The thickness of the CS/MgO-GO coating was determined by cross-section observation to be between 38–42 μm (Figure 5a). The thickness of the CS-based films with different amounts of MgO-GO fillers did not differ significantly. Surface wettability is an important factor influencing corrosion performance and bioactivity of biomaterials [33]. Contact angle measurements were used to determine the wettability of the coated and uncoated samples (Figure 5b). Bare Mg alloy and neat CS have water contact angles (WCA) of 92.3° and 84.4°, respectively. Nevertheless, the WCA of the CS/MgO-GO coating decreased from 58.7° for 1MgO-GO to 51.2° for 3MgO-GO as the concentration of MgO-GO increased. The surface wettability of the coated samples was higher than that of the uncoated Mg alloy. This behavior can be attributed to the presence of functional groups (carboxyl group, carbonyl group, and hydroxyl group) at the edges of GO, which contributes to the hydrophilicity of the coatings, as well as the hydrophilic nature of chitosan [12,33] in the CS/MgO-GO nanocomposite coatings. Furthermore, increasing the MgO-GO content of CS-based coatings improved their hydrophilicity characteristics.
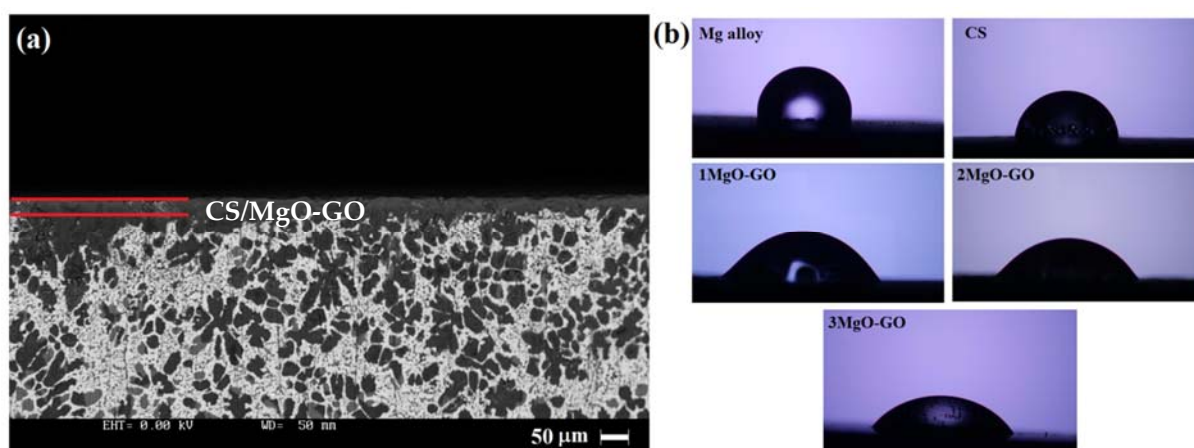

Figure 5. (**a**) Cross-section SEM image, and (**b**) images of water contact angle of uncoated, CS, CS/1MgO-GO, CS/2MgO-GO, and CS/3MgO-GO coated Mg alloys.

The adhesion test was used to evaluate the adhesion strength of the CS and CS/MgO-GO nanocomposite coatings deposited on Mg alloy. According to Figure 6, the adhesion of the CS coating on the Mg alloy was 2.64 MPa before composite coating, but this value increased to 4.42 MPa after composite coating, demonstrating the effective role of MgO-GO fillers in improving coating adhesion strength. In fact, one of the most important factors in achieving long-term implant use without premature failure *in vivo* is strong interfacial

bonding between them [22]. There are oxygen functional groups at the GO sheet's edges which can conveniently form hydrogen bonds with functional oxygen groups comprising CS. At the same time, there is strong bonding between the Mg-O and CS layer sites (=O). On the other hand, the integration of MgO-GO into the CS layer, on the other hand, has a major effect on the adhesion strength between the Mg alloy specimen and the CS/MgO-GO nanocomposite coating [22,26]. In this regard, it was reported [34] that the newly formed hydroxyl groups on the Mg alloy surface may improve coating adhesion to the substrate via chemical interaction with coating molecules.
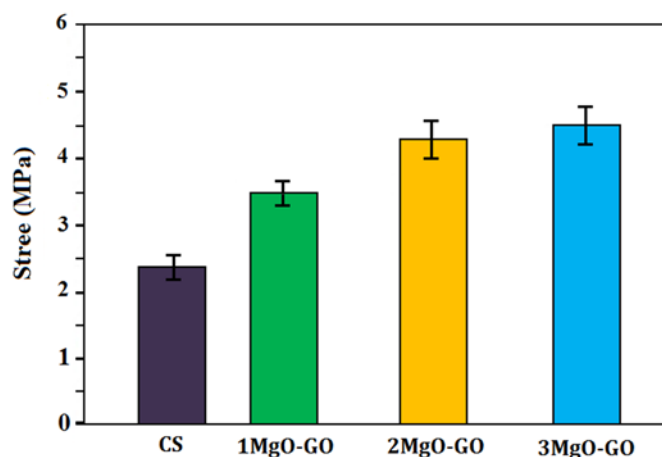

Figure 6. Bond strengths of CS, CS/1MgO-GO, CS/2MgO-GO, and CS/3MgO-GO coated Mg alloys.

3.3. Corrosion Behavior

The corrosion resistance of Mg alloy, CS, and CS/MgO-GO was evaluated in SBF using a potentiodynamic polarization test, and the corresponding polarization curves are shown in Figure 7a. When compared to Mg alloy (i_{corr} = 167.82 μA/cm^2), the i_{corr} value of CS shifted to a relatively negative position (50.22 μA/cm^2), whereas the i_{corr} value of CS/2MgO-GO presented a much lower corrosion current density (14.98 μA/cm^2) when compared to Mg alloy. The corrosion rate is known to be directly proportional to i_{corr}. Although the CS coating corroded more readily, this could be due to its porous surface with more defect structure, which increased the contact area between the corrosive fluid and the substrate [5]. The surface of the CS coating containing close pores was filled with MgO-GO fillers, resulting in improved corrosion resistance of the composite coating.

EIS analysis was carried out by generating Nyquist plots for the bare Mg, CS, and CS/MgO-GO coatings, as shown in Figure 7b. Based on the fitting results, the R$_{ct}$ values for CS (1021.5 Ω.cm^2) and CS/MgO-GO were 1536.5 Ω.cm^2 (1MgO-GO), 1808.6 Ω.cm^2 (2MgO-GO), and 1257.2 Ω.cm^2 (3MgO-GO), which were significantly higher than the bare Mg alloy (401.2 Ω.cm^2). The results confirmed the higher electrochemical impedance of the CS/MgO-GO composite coating for Mg alloy, protecting substrates from over-quick degradation. The lower R$_{ct}$ value of CS/3MgO-GO coated specimens compared to CS/2MgO-GO and CS/1MgO-GO coated samples is due to the presence of more MgO/GO aggregates in the CS/3MgO-GO film, which led to the reduction in corrosion rate. A higher value of the low-frequency impedance modulus, |Z|, indicates better corrosion protection performance [35]. As shown in Figure 7c, the value of |Z| for the CS and CS/MgO-GO coatings was greater than that of the uncoated Mg alloy. Furthermore, the phase angle (θ) at high frequency can be used to assess the completeness of the coating under the influence of corrosive electrolyte [35,36]. In Figure 7c, the phase angles of coated samples in the medium frequency range became loftier, indicating that a passivation film had formed on the surface of the samples as an inhibitor against corrosion. A complete coating has a phase angle close to 90° [37]. whereas the bare substrate has a phase angle close to 0° [37]. The uncoated has a high frequency of phase angle of 50°, demonstrating the sample's unsatisfactory integrity. The capacitance behavior of CS/MgO-GO coating has the widest

frequency range, and its phase angle is increased by approximately 60°, indicating that the formation of CS/MgO-GO coating can improve the corrosion resistance of the substrate. The equivalent is used to characterize the samples, where R_s denotes the solution resistance, CPE coat denotes the coating capacitance, R_{ct} denotes the charge transfer resistance, and CPE-dl denotes the electric double-layer capacitance of the passive film (Figure 7d). This finding indicates that the coencapsulation of MgO and GO fillers into CS film have the potential to elevate the corrosion resistance of the Mg alloy substrate.
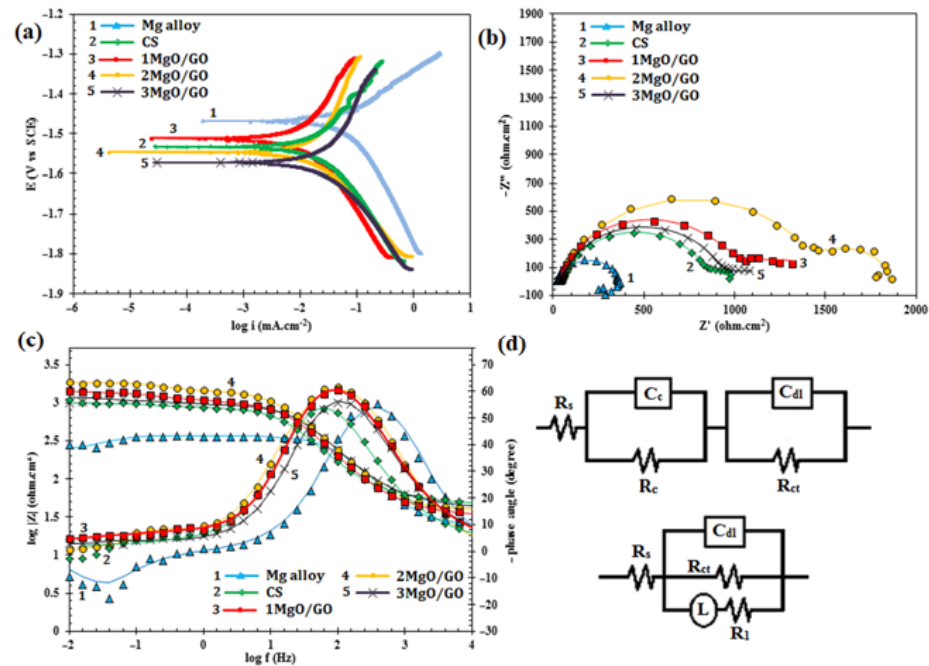

Figure 7. Electrochemical measurements of uncoated, CS, CS/1MgO-GO, CS/2MgO-GO, and CS/3MgO-GO coated Mg samples in m-SBF solution. (**a**) Potentiodynamic polarization curves; (**b**) Nyquist plots and (**c**) representative impedance (Bode magnitude and phase) spectra; and (**d**) equivalent circuit for impedance spectra.

The morphology of the surface of the various specimens after 14 days of immersion in the SBF is depicted in Figure 8a–e. After 14 days, the uncoated Mg alloy showed obvious degradation, with pitting corrosion clearly visible and a loose corrosion layer with deep cracks developing on the uncoated Mg alloy. The CS coating, on the other hand, remained intact after 14 days, with only a few surface cracks and no evidence of pitting corrosion was found. A thick layer of biomineralization was present on the surface with numerous white spherical particles, as seen in the high-magnification image. A similar biomineralization layer was observed for the CS/MgO-GO coating. The CS/MgO-GO coating's biomineralization layer was smoother with fewer defects compared to CS coating. According to the EDS spectra (Figure 8f), the precipitates layer consists of Mg, O, C, Ca, and P demonstrating the $Mg(OH)_2$ and hydroxyapatite (HAp) creation during the immersion. A large amount of mineralization layer covered the surface of the CS/MgO-GO coated film. After 14 days of immersion, CS containing GO and MgO deposited substrates show the formation of compact apatite precipitates on their surfaces. The inclusion of graphene oxide and MgO accelerate the formation of HAp on the coated surface. Surface functional groups on the surface of GO and MgO, such as –COOH and –OH, act as nucleating centers and provide a superior biomineralization process [21,22,33]. These functional groups provide negative charges on the surfaces, which encourages more Ca^{2+} cations from the SBF medium to interact electrostatically, resulting in the formation of an apatite-rich layer. Furthermore, the hydroxyl ions (OH^-) through SBF are electrically drawn to this Ca-rich positively charged surface, resulting in the precipitation of a bone apatite compound on the surfaces of the implant.
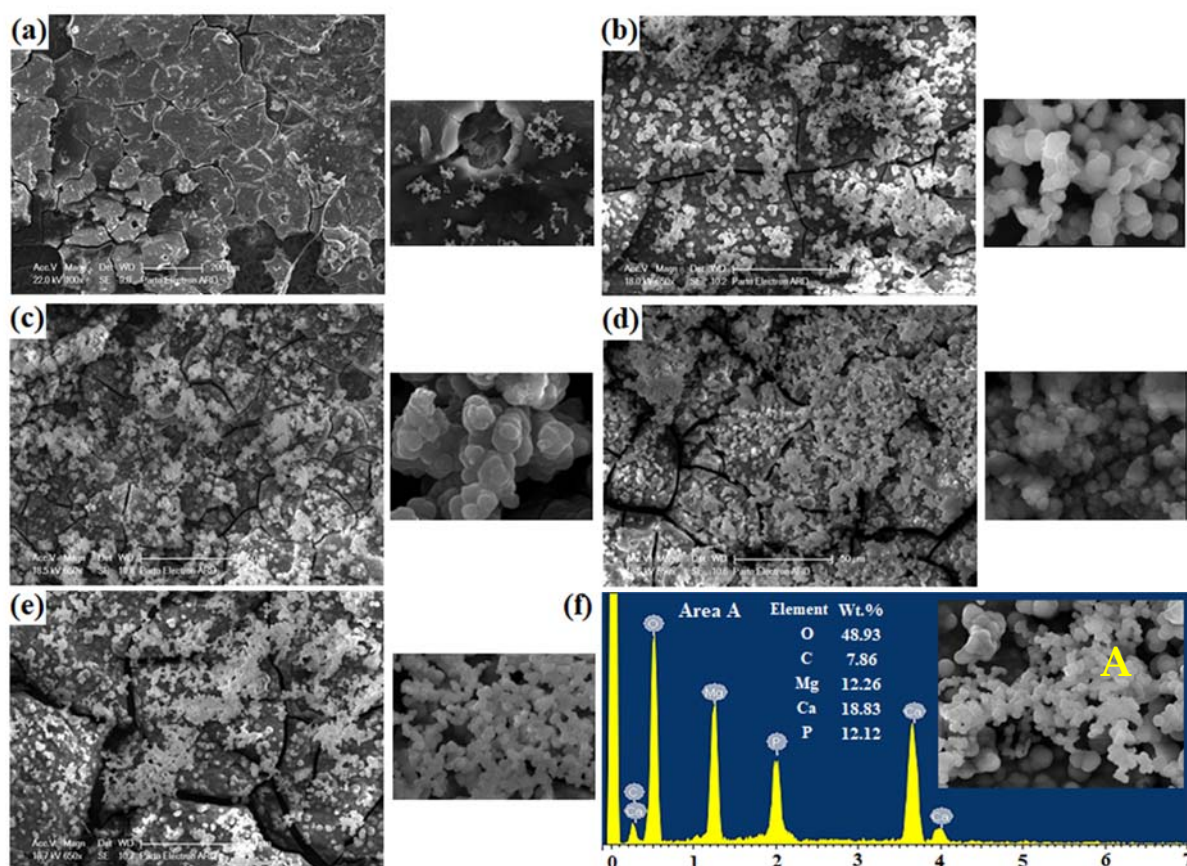
Figure 8. SEM micrographs and EDS plane-scan results of (**a**) uncoated, (**b**) CS, (**c**) CS/1MgO-GO, (**d**) CS/2MgO-GO, and (**e**) CS/3MgO-GO coated Mg samples immersed in m-SBF solution for 7 days and (**f**) EDX analysis of Area A.

During the biodegradation procedure, the coated Mg alloy had significantly lower pH values than the Mg alloy without coating. During the first 7 days, the pH value of the bare Mg alloy samples increased dramatically from 7.40 to 10.10, while the trend was reversed for the coated Mg alloy samples, particularly the CS/MgO-GO samples (Figure 9a). The pH value of the CS/MgO-GO coated Mg alloy sample increased steadily and slowly over 14 days, changing only from 7.88 to 8.76. The slope of the pH curve of the bare and coated samples decreased as the immersion time increased for all specimens. This finding may be due to the samples' reduced surface area, which delay initiation of corrosion process. During the first few days of exposure, a larger surface region was exposed to the solution, resulting in more degradation processes and the generation of hydroxide (OH) ions, increasing the pH value. However, when the exposure time was increased to 7 and 14 days, the pH value of the composites decreased and then remained stable. This phenomenon could be explained by the longer immersion time, which results in the development of protective films from corrosion products on the sample surface. These corrosion product films inhibit the specimens from coming into direct contact with the solution, lowering the pH of the specimens. Meanwhile, as shown in Figure 9b, after 14 days of immersion, the coated samples released significantly less hydrogen than the bare Mg alloy (22.8 mL/cm^2). The measured volume of hydrogen evolution for CS coated samples was 12.7 mL/cm^2, 8.8 mL/cm^2 for CS/1MgO-GO coating, and 7.9 mL/cm^2 for CS/2MgO-GO coating, all of which agreed with the pH value results. This was mainly due to the compact and protective layer of CS/MgO-GO that was effectively applied to the Mg alloy surface, which can successfully preserve the substrate from the corrosion medium and certainly decrease the hydrogen evolution rate [37]. Furthermore, the weight loss of the CS/MgO-GO sample was 0.58 mm/y, which was much lower compared to

the CS coating (1.24 mm/y) and bare Mg alloy (2.47 mm/y) (Figure 9c). These findings indicated that the CS/MgO-GO coating showed the greatest corrosion resistance even after a precise 14-day immersion test. The bare sample has the highest corrosion rate, while the coated specimen has lower corrosion rates because CS/MgO-GO acts as a barrier film and reduces the infiltration rate of corrosive solution inside the substrate, and hence decline the biodegradation rate. Furthermore, the existence of MgO particles and GO within the CS film can operate as a reinforcing agent, increasing the coating layer's stability. Furthermore, these particles promote the formation of corrosion products containing hydroxyapatite, which slows the penetration of SBF to the substrate, and provide protection resulted in slowing the degradation rate. XRD spectra for the composite coating were used to confirm the precipitation of HAp on the surface of the composite coating containing GO and MgO, as shown in Figure 9d. The XRD pattern of the CS/MgO-GO composite coatings verify that the corrosion products were primarily composed of $Mg(OH)_2$ and HAp, implying that the biomineralization layer was primarily containing HAp.
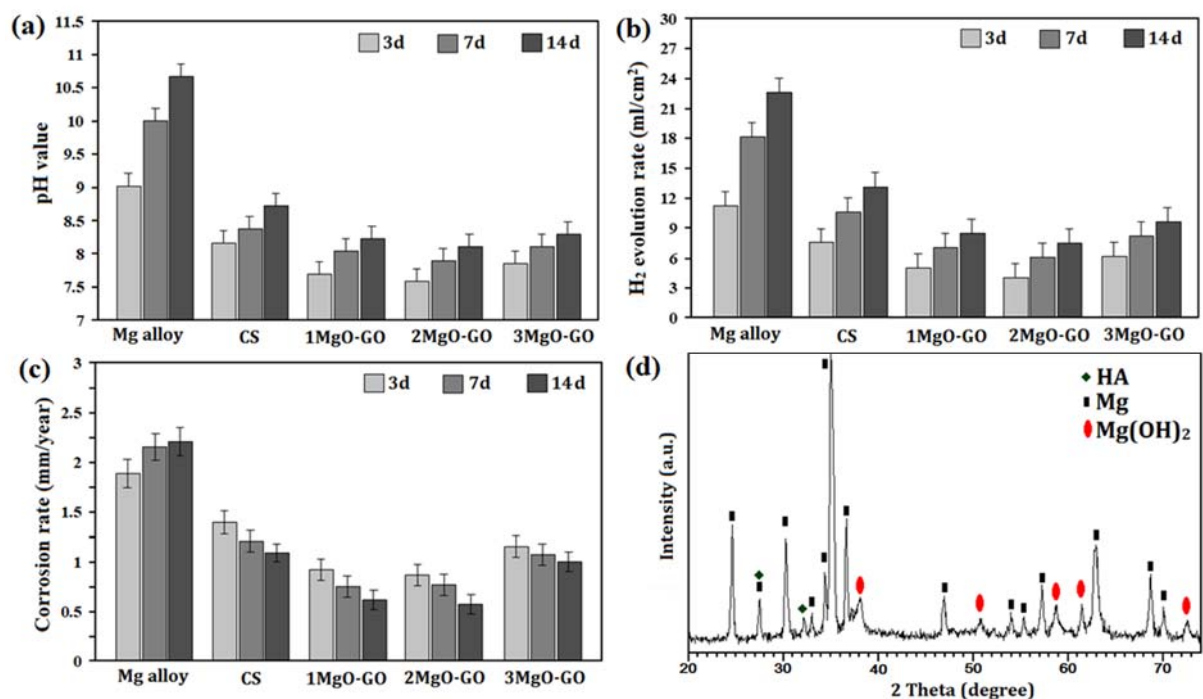

Figure 9. (**a**) pH value, (**b**) hydrogen evolution, (**c**) corrosion rate for uncoated Mg alloy, CS, CS/1MgO-GO, CS/2MgO-GO, and CS/3MgO-GO coated Mg samples coated Mg alloys versus soaking time in SBF. (**d**) X-ray diffraction patterns of CS/3MgO-GO coated Mg alloy after soaking in SBF.

3.4. Antibacterial Effect

The ability of the produced coatings to inhibit gram-negative (*Escherichia coli*) bacteria was investigated through direct contact with an agar medium. The results showed that the CS/MgO-GO coatings on Mg alloy substrates inhibited the bacterial activity of the strains (Figure 10). In comparison to the large inhibition area created for gram (−) bacteria (5.3 mm), neither the bare Mg alloy samples nor the coatings with CS coating successfully inhibited bacterial growth, even though, as reported in the literature, CS could possess antibacterial properties [8,38]. The low concentration of chitosan in the coatings may have influenced the results [38]. At the same time, the zones of antibacterial activity against *E. coli* colonies increased in the sequence of bare Mg alloy < CS < CS/1MgO-GO < CS/2MgO-GO < CS/3MgO-GO. The release of MgO and GO has a strong inhibitory effect on bacterial growth. When bacterial cells come into contact with MgO and GO, they are eventually destroyed due to various mechanisms such as oxidative stress, membrane

stress, and/or wrapping isolation. Bacterial growth will be inhibited bacteriostatically or bactericidal by these mechanisms, which may operate independently or in combination [26]. Among the various suggested mechanisms for GO's antimicrobial performance, mechanical destruction to bacteria membranes through sharp edges of GO when contacting directly with GO and the formation of reactive oxygen species (ROS) occurred when oxidative stress generated by GO and charge transfer are more circumstances [7,39]. MgO as another antibacterial agent reacts with intracellular oxygen to produce ROS such as H_2O_2, $OH^\bullet$ and $O_2^{\bullet-}$, which may be released into the medium and thus inhibit bacterial proliferation and growth [19,26]. Consequently, co-encapsulation of MgO-GO into the CS layer surface significantly inhibited the bacterial activity of the strains; thus, CS/MgO-GO coating containing the highest amount of MgO-GO showed the best antibacterial activity.
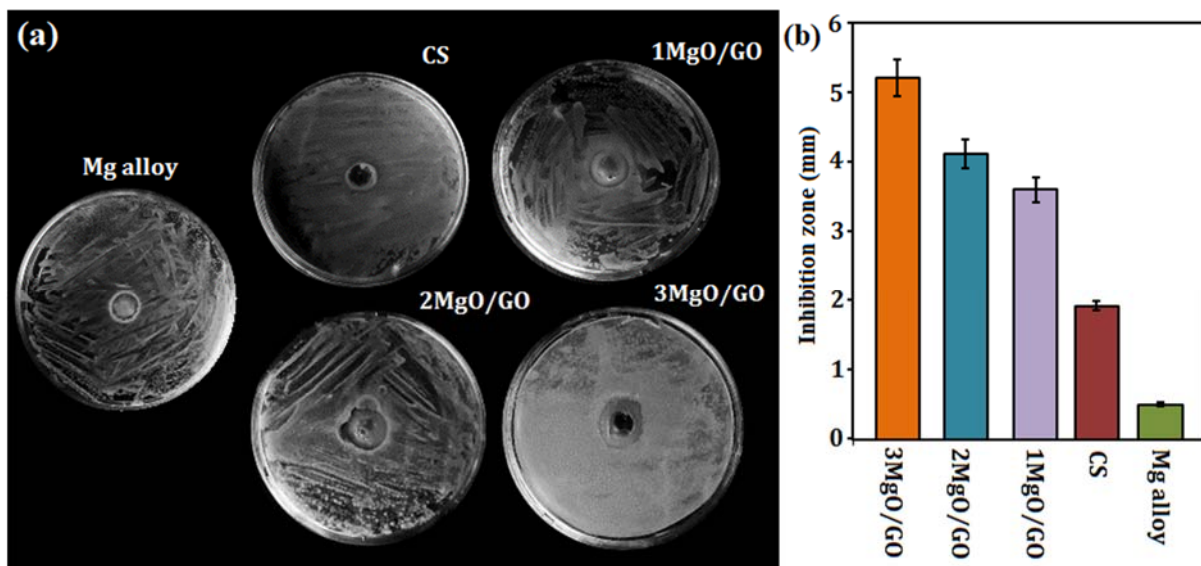

Figure 10. (**a**) Images of inhibition zones, and (**b**) values of growth-inhibition zones of uncoated Mg alloy, CS, CS/1MgO-GO, CS/2MgO-GO, and CS/3MgO-GO coated Mg samples after 24 h.

3.5. Cytotoxicity Assay

The MG63 cell response to uncoated, CS, and CS/MgO-GO coated samples was evaluated using an indirect assay. Figure 11a illustrates the changes in cell viability as a function of culture time. All extracts of CS/MgO-GO coated Mg alloy enhanced the cell viability of MG-63 cells compared to the uncoated ones. Similarly, cells contacted with all extracts of CS and CS/MgO-GO coated specimens showed low cytotoxicity after 3 and 5 days of culture, whereas that was exacerbated by extending the culture time in uncoated. Cells incubated with extract of CS/2MgO-GO coated had significantly higher viability on day 3 (91% $\pm$ 4%) and day 5 (98% $\pm$ 4%). Compared to the other three CS/MgO-GO groups. However, there was no statistical diversity ($p > 0.05$) in MG63 cell viability between the CS/MgO-GO groups after 5 days, despite a slight trend toward increased cell viability in the uncoated group. The surface oxygen-containing functional groups of GO may stimulate cell attachment [40]. According to Depan et al. [41], the hydroxyl groups on GO can serve as locations for preserving and bringing cells onto fibrous surfaces, thereby improving cell adhesion. Similarly, Shuai et al. [42] demonstrated that GO could be used to create a bio-interface for cell proliferation and growth. One of the most widely used indicators of osteoblast cell differentiation is ALP activity. The ALP activity of the MG-63 cell line cultured in media of the uncoated extract, CS, and CS/MgO-GO coated samples is shown in Figure 11b. For 3 and 7 days of culture, the CS and CS/MgO-GO coated samples demonstrated good cell differentiation than the uncoated sample. After 7 days, the ALP activity of all samples increased noticeably. Furthermore, the CS/2MgO-GO coated specimen demonstrated the greatest ALP activity at both time points tested, implying a

greater potential for cell differentiation. The increased corrosion rate in uncoated Mg alloys resulted in a greater release of Mg ions [43–52], causing the culture medium to become excessively alkalinization and local hydrogen evolution. All of these were detrimental to cell differentiation. Modification with the CS/MgO-GO composite coating, on the other hand, improved corrosion resistance of the substrate while providing a quite favorable surrounding for cell differentiation.
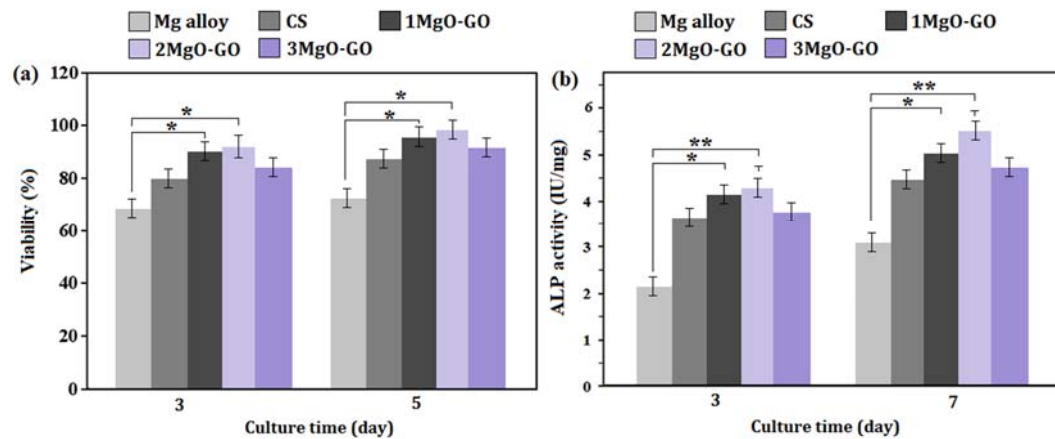

Figure 11. (**a**) Cell viability, and (**b**) ALP activity of MG63 cells cultured for various times on uncoated Mg, and Mg alloys coated with CS, CS/1MgO-GO, CS/2MgO-GO, and CS/3MgO-GO (* $p < 0.05$, and ** $p < 0.01$).

4. Conclusions

A novel CS/MgO-GO composite coating was deposited on a biodegradable Mg alloy in this study. The results of the electrochemical analysis showed that the i_{corr} values of CS (50.22 μA/cm^2) are lower compare with uncoated Mg alloy (167.82 μA/cm^2). After the addition of MgO and GO into the CS film, the i_{corr} value of CS/2MgO-GO was 14.98 μA/cm^2, further reduced relative to that of CS/3MgO-GO coating. This finding indicates that the coencapsulation of MgO and GO fillers into CS film has the potential to elevate the corrosion resistance of the Mg alloy substrate. The immersion test including H$_2$ evolution and weight loss indicates that the CS/MgO-GO composite coating may greatly enhance the corrosion resistance of Mg alloys. Meanwhile, after 14 days of immersion in SBF, apatite was observed on the coating surface, implying that incorporating MgO and GO in the CS film could enhance apatite formation and improve the Mg alloy bioactivity. The cytotoxicity study showed that the CS/MgO-GO composite coating improved the biocompatibility of Mg alloy substrates. Besides, the formation of apatite precipitate on the surface of the sample leads to a reduction of the degradation rate of Mg alloys. The coencapsulation of MgO and GO fillers into the CS coatings effectively enhances the antibacterial activity of Mg alloy. This research could provide a plausible and encouraging approach for preserving corrosion resistance while improving the biocompatibility and antibacterial properties of Mg alloy implants.

Author Contributions: Methodology, formal analysis, writing—original draft preparation, M.Z.B., S.A. and A.N.; Conceptualization, supervision, visualization, writing—review and editing, A.F.I., S.S. and H.R.B.-R.; supervision, visualization, writing—review and editing, funding acquisition, S.R., M.D. and F.B. All authors have read and agreed to the published version of the manuscript.

Institutional Review Board Statement: Not applicable.

Informed Consent Statement: Not applicable.

Data Availability Statement: All data provided in the present manuscript are available to whom it may concern.

Conflicts of Interest: The funders had no role in the design of the study; in the collection, analyses, or interpretation of data; in the writing of the manuscript, or in the decision to publish the results.

References

1. Chen, Y.; Wu, L.; Yao, W.; Chen, Y.; Zhong, Z.; Ci, W.; Wu, J.; Xie, Z.; Yuan, Y.; Pan, F. A self-healing corrosion protection coating with graphene oxide carrying 8-hydroxyquinoline doped in layered double hydroxide on a micro-arc oxidation coating. *Corros. Sci.* **2022**, *194*, 109941. [CrossRef]
2. Francis, A.; Yang, Y.; Boccaccini, A. A new strategy for developing chitosan conversion coating on magnesium substrates for orthopedic implants. *Appl. Surf. Sci.* **2019**, *466*, 854–862. [CrossRef]
3. Zhou, Z.; Zheng, B.; Gu, Y.; Shen, C.; Wen, J.; Meng, Z.; Chen, S.; Ou, J.; Qin, A. New approach for improving anticorrosion and biocompatibility of magnesium alloys via polydopamine intermediate layer-induced hydroxyapatite coating. *Surf. Interfaces* **2020**, *19*, 100501. [CrossRef]
4. Yang, Y.; Michalczyk, C.; Singer, F.; Virtanen, S.; Boccaccini, A.R. In vitro study of polycaprolactone/bioactive glass composite coatings on corrosion and bioactivity of pure Mg. *Appl. Surf. Sci.* **2015**, *355*, 832–841. [CrossRef]
5. Tian, P.; Liu, X.; Ding, C. In vitro degradation behavior and cytocompatibility of biodegradable AZ31 alloy with PEO/HT composite coating. *Colloids Surf. B Biointerfaces* **2015**, *128*, 44–54. [CrossRef] [PubMed]
6. Tiyyagura, H.R.; Rudolf, R.; Gorgieva, S.; Fuchs-Godec, R.; Boyapati, V.R.; Mantravadi, K.M.; Kokol, V. The chitosan coating and processing effect on the physiological corrosion behaviour of porous magnesium monoliths. *Prog. Org. Coat.* **2016**, *99*, 147–156. [CrossRef]
7. Pan, C.; Zhao, Y.; Yang, Y.; Yang, M.; Hong, Q.; Yang, Z.; Zhang, Q. Immobilization of bioactive complex on the surface of magnesium alloy stent material to simultaneously improve anticorrosion, hemocompatibility and antibacterial activities. *Colloids Surf. B Biointerfaces* **2021**, *199*, 111541. [CrossRef]
8. Li, J.; Zhuang, S. Antibacterial activity of chitosan and its derivatives and their interaction mechanism with bacteria: Current state and perspectives. *Eur. Polym. J.* **2020**, *138*, 109984. [CrossRef]
9. Rastegari, S.; Salahinejad, E. Surface modification of Ti-6Al-4V alloy for osseointegration by alkaline treatment and chitosan-matrix glass-reinforced nanocomposite coating. *Carbohydr. Polym.* **2019**, *205*, 302–311. [CrossRef]
10. Saadati, A.; Khiarak, B.N.; Zahraei, A.A.; Nourbakhsh, A.; Mohammadzadeh, H. Electrochemical characterization of Electrophoretically deposited Hydroxyapatite/Chitosan/Graphene Oxide composite coating on Mg substrate. *Surf. Interfaces* **2021**, *25*, 101290. [CrossRef]
11. Bakhsheshi-Rad, H.R.; Chen, X.; Ismail, A.F.; Aziz, M.; Abdolahi, E.; Mahmoodiyan, F. Improved antibacterial properties of an Mg-Zn-Ca alloy coated with chitosan nanofibers incorporating silver sulfadiazine multiwall carbon nanotubes for bone implants. *Polym. Adv. Technol.* **2019**, *30*, 1333–1339. [CrossRef]
12. Askarnia, R.; Fardi, S.R.; Sobhani, M.; Staji, H. Ternary hydroxyapatite/chitosan/graphene oxide composite coating on AZ91D magnesium alloy by electrophoretic deposition. *Ceram. Int.* **2021**, *47*, 27071–27081. [CrossRef]
13. Avcu, E.; Baştan, F.E.; Abdullah, H.Z.; Rehman, M.A.U.; Avcu, Y.Y.; Boccaccini, A.R. Electrophoretic deposition of chitosan-based composite coatings for biomedical applications: A review. *Prog. Mater. Sci.* **2019**, *103*, 69–108. [CrossRef]
14. Güler, Ö.; Bağcı, N. A short review on mechanical properties of graphene reinforced metal matrix composites. *J. Mater. Res. Technol.* **2020**, *9*, 6808–6833. [CrossRef]
15. Karimi, N.; Kharaziha, M.; Raeissi, K. Electrophoretic deposition of chitosan reinforced graphene oxide-hydroxyapatite on the anodized titanium to improve biological and electrochemical characteristics. *Mater. Sci. Eng. C* **2019**, *98*, 140–152. [CrossRef] [PubMed]
16. Khalajabadi, S.Z.; Kadir, M.R.A.; Izman, S.; Bakhsheshi-Rad, H.R.; Farahany, S. Effect of mechanical alloying on the phase evolution, microstructure and bio-corrosion properties of a Mg/HA/TiO$_2$/MgO nanocomposite. *Ceram. Int.* **2014**, *40*, 16743–16759. [CrossRef]
17. Shuai, C.; Wang, B.; Bin, S.; Peng, S.; Gao, C. Interfacial strengthening by reduced graphene oxide coated with MgO in biodegradable Mg composites. *Mater. Des.* **2020**, *191*, 108612. [CrossRef]
18. Shuai, C.; Zan, J.; Qi, F.; Wang, G.; Liu, Z.; Yang, Y.; Peng, S. nMgO-incorporated PLLA bone scaffolds: Enhanced crystallinity and neutralized acidic products. *Mater. Des.* **2019**, *174*, 107801. [CrossRef]
19. Raveesha, H.; Nayana, S.; Vasudha, D.; Begum, J.S.; Pratibha, S.; Ravikumara, C.; Dhananjaya, N. The electrochemical behavior, antifungal and cytotoxic activities of phytofabricated MgO nanoparticles using Withania somnifera leaf extract. *J. Sci. Adv. Mater. Devices* **2019**, *4*, 57–65. [CrossRef]
20. Rahnamaee, S.Y.; Bagheri, R.; Heidarpour, H.; Vossoughi, M.; Golizadeh, M.; Samadikuchaksaraei, A. Nanofibrillated chitosan coated highly ordered titania nanotubes array/graphene nanocomposite with improved biological characters. *Carbohydr. Polym.* **2021**, *254*, 117465. [CrossRef]

21. Munir, K.S.; Wen, C.; Li, Y. Carbon nanotubes and graphene as nanoreinforcements in metallic biomaterials: A review. *Adv. Biosyst.* **2019**, *3*, 1800212. [CrossRef]

22. Shahin, M.; Wen, C.; Munir, K.; Li, Y. Mechanical and corrosion properties of graphene nanoplatelet–reinforced Mg–Zr and Mg–Zr–Zn matrix nanocomposites for biomedical applications. *J. Magnes. Alloy.* **2021**. [CrossRef]

23. Bakhsheshi-Rad, H.R.; Hamzah, E.; Daroonparvar, M.; Saud, S.N.; Abdul-Kadir, M.R. Bi-layer nano-TiO_2/FHA composite coatings on Mg–Zn–Ce alloy prepared by combined physical vapour deposition and electrochemical deposition methods. *Vacuum* **2014**, *110*, 127–135. [CrossRef]

24. Yu, H.; Zhang, B.; Bulin, C.; Li, R.; Xing, R. High-efficient Synthesis of Graphene Oxide Based on Improved Hummers Method. *Sci. Rep.* **2016**, *6*, 36143. [CrossRef] [PubMed]

25. Guo, T.; Bulin, C. Facile preparation of MgO/graphene oxide nanocomposite for efficient removal of aqueous Congo red: Adsorption performance and interaction mechanism. *Res. Chem. Intermed.* **2021**, *47*, 945–971. [CrossRef]

26. Bakhsheshi-Rad, H.R.; Ismail, A.F.; Aziz, M.; Akbari, M.; Hadisi, Z.; Khoshnava, S.M.; Pagan, E.; Chen, X. Co-incorporation of graphene oxide/silver nanoparticle into poly-L-lactic acid fibrous: A route toward the development of cytocompatible and antibacterial coating layer on magnesium implants. *Mater. Sci. Eng. C.* **2020**, *111*, 110812. [CrossRef] [PubMed]

27. Abdel-Aal, S.K.; Ionov, A.; Mozhchil, R.N.; Naqvi, A.H. Simple synthesis of graphene nanocomposites MgO–rGO and Fe_2O_3–rGO for multifunctional applications. *Appl. Phys. A* **2018**, *124*, 365. [CrossRef]

28. Bordbar-Khiabani, A.; Ebrahimi, S.; Yarman, B. Highly corrosion protection properties of plasma electrolytic oxidized titanium using rGO nanosheets. *Appl. Surf. Sci.* **2019**, *486*, 153–165. [CrossRef]

29. Duan, J.; Liu, F.; Kong, Y.; Hao, M.; He, J.; Wang, J.; Wang, S.; Liu, H.; Sang, Y. Homogeneous Chitosan/Graphene Oxide Nanocomposite Hydrogel-Based Actuator Driven by Efficient Photothermally Induced Water Gradients. *ACS Appl. Nano Mater.* **2020**, *3*, 1002–1009. [CrossRef]

30. Li, H.; Lu, S.; Qin, W.; Wu, X. In-situ grown MgO-ZnO ceramic coating with high thermal emittance on Mg alloy by plasma electrolytic oxidation. *Acta Astronaut.* **2017**, *136*, 230–235. [CrossRef]

31. Liu, L.; Peng, F.; Zhang, D.; Li, M.; Huang, J.; Liu, X. A tightly bonded reduced graphene oxide coating on magnesium alloy with photothermal effect for tumor therapy. *J. Magnes. Alloy.* **2021**. [CrossRef]

32. Pishbin, F.; Mouriño, V.; Flor, S.; Kreppel, S.; Salih, V.; Ryan, M.P.; Boccaccini, A.R. Electrophoretic deposition of gentamicin-loaded bioactive glass/chitosan composite coatings for orthopaedic implants. *ACS Appl. Mater. Interfaces* **2014**, *6*, 8796–8806. [CrossRef]

33. Baradaran, S.; Moghaddam, E.; Basirun, W.J.; Mehrali, M.; Sookhakian, M.; Hamdi, M.; Moghaddam, M.R.N.; Alias, Y. Mechanical properties and biomedical applications of a nanotube hydroxyapatite-reduced graphene oxide composite. *Carbon* **2014**, *69*, 32–45. [CrossRef]

34. Asadi, H.; Suganthan, B.; Ghalei, S.; Handa, H.; Ramasamy, R.P. A multifunctional polymeric coating incorporating lawsone with corrosion resistance and antibacterial activity for biomedical Mg alloys. *Prog. Org. Coat.* **2021**, *153*, 106157. [CrossRef]

35. Kartsonakis, I.; Balaskas, A.; Koumoulos, E.; Charitidis, C.; Kordas, G. Evaluation of corrosion resistance of magnesium alloy ZK10 coated with hybrid organic–inorganic film including containers. *Corros. Sci.* **2012**, *65*, 481–493. [CrossRef]

36. Wang, C.; Fang, H.; Qi, X.; Hang, C.; Sun, Y.; Peng, Z.; Wei, W.; Wang, Y. Silk fibroin film-coated MgZnCa alloy with enhanced in vitro and in vivo performance prepared using surface activation. *Acta Biomater.* **2019**, *91*, 99–111. [CrossRef] [PubMed]

37. Guo, Y.; Jia, S.; Qiao, L.; Su, Y.; Gu, R.; Li, G.; Lian, J. Enhanced corrosion resistance and biocompatibility of polydopamine/dicalcium phosphate dihydrate/collagen composite coating on magnesium alloy for orthopedic applications. *J. Alloy. Compd.* **2020**, *817*, 152782. [CrossRef]

38. Ballarre, J.; Aydemir, T.; Liverani, L.; Roether, J.A.; Goldmann, W.H.; Boccaccini, A.R. Versatile bioactive and antibacterial coating system based on silica, gentamicin, and chitosan: Improving early stage performance of titanium implants. *Surf. Coat. Technol.* **2020**, *381*, 125138. [CrossRef]

39. Hegab, H.M.; ElMekawy, A.; Zou, L.; Mulcahy, D.; Saint, C.; Ginic-Markovic, M. The controversial antibacterial activity of graphene-based materials. *Carbon* **2016**, *105*, 362–376. [CrossRef]

40. Kim, J.D.; Yun, H.; Kim, G.C.; Lee, C.W.; Choi, H.C. Antibacterial activity and reusability of CNT-Ag and GO-Ag nanocomposites. *Appl. Surf. Sci.* **2013**, *283*, 227–233. [CrossRef]

41. Depan, D.; Girase, B.; Shah, J.S.; Misra, R.D.K. Structure–process–property relationship of the polar graphene oxide-mediated cellular response and stimulated growth of osteoblasts on hybrid chitosan network structure nanocomposite scaffolds. *Acta Biomater.* **2011**, *7*, 3432–3445. [CrossRef]

42. Shuai, C.; Guo, W.; Wu, P.; Yang, W.; Hu, S.; Xia, Y.; Feng, P. A graphene oxide-Ag co-dispersing nanosystem: Dual synergistic effects on antibacterial activities and mechanical properties of polymer scaffolds. *Chem. Eng. J.* **2018**, *347*, 322–333. [CrossRef]

43. Dziková, J.; Fintová, S.; Kajánek, D.; Florková, Z.; Wasserbauer, J.; Doležal, P. Characterization and corrosion properties of fluoride conversion coating prepared on AZ31 magnesium alloy. *Coatings* **2021**, *11*, 675. [CrossRef]

44. Wang, Z.; Ye, F.; Chen, L.; Lv, W.; Zhang, Z.; Zang, Q.; Peng, J.; Sun, L.; Lu, S. Preparation and Degradation Characteristics of MAO/APS Composite Bio-Coating in Simulated Body Fluid. *Coatings* **2021**, *11*, 667. [CrossRef]

45. Anawati, A.; Fitriana, M.; Gumelar, M. Improved Corrosion Resistance of Magnesium Alloy AZ31 in Ringer Lactate by Bilayer Anodic Film/Beeswax–Colophony. *Coatings* **2021**, *11*, 564. [CrossRef]

46. Wei, J.; Cai, S.; Li, Q.; Xie, Y.; Bao, X.; Xu, G. Controllable Synthesis of Nanostructured Ca-P Coating on Magnesium Alloys via Sodium Citrate Template-Assisted Hydrothermal Method and Its Corrosion Resistance. *Coatings* **2020**, *10*, 1232. [CrossRef]

47. Zhang, R.; Zhang, Z.; Zhu, Y.; Zhao, R.; Zhang, S.; Shi, X.; Li, G.; Chen, Z.; Zhao, Y. Degradation Resistance and In Vitro Cytocompatibility of Iron-Containing Coatings Developed on WE43 Magnesium Alloy by Micro-Arc Oxidation. *Coatings* **2020**, *10*, 1138. [CrossRef]

48. Toulabifard, A.; Rahmati, M.; Raeissi, K.; Hakimizad, A.; Santamaria, M. The Effect of Electrolytic Solution Composition on the Structure, Corrosion, and Wear Resistance of PEO Coatings on AZ31 Magnesium Alloy. *Coatings* **2020**, *10*, 937. [CrossRef]

49. Wang, S.; Fu, L.; Nai, Z.; Liang, J.; Cao, B. Comparison of Corrosion Resistance and Cytocompatibility of MgO and ZrO$_2$ Coatings on AZ31 Magnesium Alloy Formed via Plasma Electrolytic Oxidation. *Coatings* **2018**, *8*, 441. [CrossRef]

50. Hou, S.; Yu, W.; Yang, Z.; Li, Y.; Yang, L.; Lang, S. Properties of Titanium Oxide Coating on MgZn Alloy by Magnetron Sputtering for Stent Application. *Coatings* **2020**, *10*, 999. [CrossRef]

51. Li, S.; Yi, L.; Zhu, X.; Liu, T. Ultrasonic Treatment Induced Fluoride Conversion Coating without Pores for High Corrosion Re-sistance of Mg Alloy. *Coatings* **2020**, *10*, 996. [CrossRef]

52. Fu, L.; Yang, Y.; Zhang, L.; Wu, Y.; Liang, J.; Cao, B. Preparation and Characterization of Fluoride-Incorporated Plasma Electrolytic Oxidation Coatings on the AZ31 Magnesium Alloy. *Coatings* **2019**, *9*, 826. [CrossRef]